Particle image velocimetry in the impeller of a centrifugal pump: a POD-based analysis

William D. P. Fonseca*[a], Rafael F. L. Cerqueira[b,c], Rodolfo M. Perissinotto[b], William Monte Verde[b], Marcelo S. Castro[a,b], Erick M. Franklin[a]

[a] *School of Mechanical Engineering, University of Campinas, Campinas - SP, Brazil*
[b] *Center for Energy and Petroleum Studies, University of Campinas, Campinas - SP, Brazil*
[c] *Mechanical Engineering Department, Federal University of Santa Catarina, Florianopolis - SC, Brazil*

Abstract

The flow field within the channels of a centrifugal pump impeller is usually complex, containing turbulent structures in a wide range of time and length scales. Identifying the different structures and their dynamics in this rotating frame is, therefore, a difficult task. However, modal decomposition can be a useful tool for detecting coherent structures. In this paper, we make use of proper orthogonal decomposition (POD) of time-resolved flow fields in order to investigate the flow in a centrifugal pump. For that, we carried out experiments using time-resolved particle image velocimetry (TR-PIV) in a pump of transparent material operating at different conditions and obtained the statistical characteristics of the turbulent flow from phase-ensemble averages of velocities and turbulent kinetic energy. The results reveal that at the pump's best efficiency point (BEP) the flow is well-organized, with no significant flow separation. For flow rates below the BEP, flow separation and vortex structures appear in the impeller channels, making the flow unstable. At flow rates above the BEP, intense jets appear close to the suction blades, while small instabilities occur on the pressure side. The POD analysis shows that at low flow rates, the flow is dominated by large-scale structures with intense energy levels, while at the BEP and higher flow rates, the flow is dominated by small-scale structures. Our results shed light on the turbulence characteristics inside the impeller, providing relevant information for reduced-order models capable of computing the flow in turbomachinery at much lower costs when compared to traditional methods.

Keywords: `POD, PIV, centrifugal pump, impeller`

*Corresponding author: William D. P. Fonseca fonsecawdp@gmail.com

1. Introduction

Centrifugal pumps are widely used in different industrial processes, including agricultural irrigation, water supply, oil facilities, thermal power plants, chemical, nuclear, among other applications. Although ubiquitous in industry, the flow structure in the impeller, which is the core component of the centrifugal pump, is not fully understood, being highly complex at off-design conditions. At these conditions, the flow usually contains high temporal and spatial velocity gradients, regions with strong vorticity, flow separation zones, and intense turbulence levels [1]. Therefore, a better understanding of the flow structures occurring at different operating conditions is important for designing, assembling and operating centrifugal pumps.

One way to have access to details of the flow fields in pumps is through optical techniques. Flow visualization investigations, mainly using particle image velocimetry (PIV), were carried out over the last years, and they focused generally on the main flow. Paone et al. [2] were the pioneers in the use of PIV for investigating the flow in a centrifugal pump, and they determined the fields of relative velocity and vorticity in a pump diffuser. Their work was expanded by Dong et al. [3, 4], who estimated momentum and energy fluxes, turbulent stresses, and turbulence production in a pump volute. Later, Sinha and Katz [5] conducted experiments to investigate the flow in the gap between the pump impeller and diffuser. The authors identified the formation of turbulent structures, such as jets and wakes related to velocity fluctuations. Furthermore, the authors concluded that the rotating impeller of a centrifugal pump may promote the occurrence of hydrodynamic instabilities which affect the structure of the boundary layers in the blade walls, occasionally causing the separation of the flow.

The visualization of single-phase flows in rotating impellers was also explored by Pedersen et al. [6], who carried out experiments using laser doppler velocimetry (LDV) and PIV in a transparent centrifugal pump to investigate the unsteady flow structures and turbulence characteristics. In general, the results from LDV and PIV were similar between them, but the PIV presented two advantages over the LDV: a considerably lower run time and an the ability to identify instantaneous spatial flow structures. The authors concluded that the PIV is efficient in acquiring reliable and detailed data of velocity fields inside impeller channels, especially when fluorescent particles are used as tracers. In addition, they identified that at the lowest flow rates, intense instabilities arise in the diffuser and then spread to the impeller, leading to the prevalence of unsteady flow patterns.

Krause et al. [7] and Zhang et al. [8] characterized the evolution of fields of time-dependent water flows by using a time-resolved PIV system (TR-PIV). Basically, the authors obtained velocities and streamlines that revealed the formation and propagation of vortices in a radial impeller [7] and around the volute tongue region [8]. A time-resolved approach was also adopted by Mittag and Gabi [9] for studying the flow of a mineral oil in the intake and impeller of a transparent centrifugal pump. The main advantage of using mineral oils in transparent pumps is basically the refractive index, which present close values for the fluid and the acrylic material used in the pump structure.

More recently, Keller et al. [10] executed one of the most extensive investigations on single-phase flows in pumps. For the flow rate corresponding to the best efficiency point (BEP), the authors noticed that a vorticity sheet of high intensity occurs in the suction blade of the impeller as a consequence of velocity gradients. Besides, a negative (or inverted sign) vorticity sheet and an intense turbulent kinetic energy production zone were detected in the blade trailing edge. In addition to the studies reported above, it is important to mention that significant attention has been devoted to visualize the internal flow in centrifugal pumps with either vaned [11, 12, 13] or vaneless diffusers [14, 15, 16], as well as to study other phenomena such as the influence of flow patterns on the hydraulic performance [17, 18, 19, 20, 21].

As the flow field in the impeller of a centrifugal pump is highly complex, traditional analysis based on the raw data are unable to reveal the dominant unsteady flow structure efficiently [22]. In this context, the proper orthogonal decomposition (POD) method has received increasing attention for analyzing complex fields. After Lumley [23] successfully applied the POD method on the study of turbulence, it remained one of the most widely used techniques and evolved in multiple forms [24, 25, 26, 27, 28]. For example, Ma and Karniadakis [29], Liberge and Hamdouni [30] and El-Adawy et al. [31] investigated flow in cylinders, a classic fluid mechanics problem, demonstrating that the POD technique could precisely describe its characteristics. POD was also applied in the analyses of engines [32, 33], compressors [34], centrifugal fans [35] and jets [36, 37, 38, 39].

Nevertheless, few studies regarding the use of the POD in centrifugal pumps have been carried out so far, and all of them numerically. Zhang et al. [40] used POD to improve the accuracy and reduce the calculation costs for the inverse problem of the flow in the impeller of a centrifugal pump. Guo et al. [41] analyzed the interrelations among impeller blade geometry, flow field fluctuation intensity, and impeller-induced hydrodynamic noise of centrifugal pump based on results from computational fluid dynamcs (CFD). Finally, making use of detached eddy simulation, Zhang et

al. [42] investigated the flow characteristics and the relationship between the hydraulic performance and energy distribution of internal flow structures in single-stage centrifugal pumps.

In this paper, we investigate the flow in a centrifugal pump by making use of proper orthogonal decomposition of time-resolved flow fields. For that, we carried out experiments using time-resolved particle image velocimetry (TR-PIV) in a pump of transparent material operating at different conditions, and obtained the statistical characteristics of the turbulent flow from phase-ensemble averages of velocities and turbulent kinetic energy. The results reveal that at the pump's best efficiency point (BEP) the flow is well-organized, with no significant flow separation. For flow rates below the BEP, flow separation and vortex structures appear in the impeller channels, making the flow unstable. At flow rates above the BEP, intense jets appear close to the suction blades, while small instabilities occur on the pressure side. The POD analysis shows that at low flow rates the flow is dominated by large-scale structures with intense energy levels, while at the BEP and higher flow rates the flow is dominated by small-scale structures. Our results shed light on the turbulence characteristics inside the impeller, providing relevant information for reduced-order models capable of computing the flow in turbomachinery at much lower costs when compared to traditional methods.

In the following, Secs. 2 and 3 present, respectively, the experimental setup and procedure and the equations governing the POD technique. Section 4 presents the results for the phase-ensemble averaged velocity fields, phase-ensemble averaged turbulent kinetic energy fields, and POD analysis of flow field. Section 5 discusses the conclusions.

2. Experiments

2.1. Transparent pump and test bench

To enable PIV measurements in the whole impeller, a prototype of a centrifugal pump with spiral volute was designed and manufactured out of a transparent material for flow visualization purposes. Further details on the prototype are available in Perissinotto et al. [43, 44].

The impeller has a radial geometry with seven channels of constant height and low aspect ratio (about $h/d_2 \approx 5\%$). The outer radius is 55 mm and the inner radius 22 mm to reduce the three-dimensional flow effects. Thus, the impeller has a geometry similar to that used by Monte Verde et al. [45] and Perissinotto et al. [46, 47] in their experiments. The main impeller parameters are shown in Tab. 1.

The working fluid enters the pump stage through four intake ports placed on the side of the pump body. The liquid then flows to the impeller inlet, traverses the channels, and finally goes to the volute before leaving the pump. The outflow direction is perpendicular to the axis of the pump shaft. The impeller is connected to the central shaft through screws and threads. In order to reduce the diffuse reflection during the experiments, the impeller hub and volute background are both made of matte black anodized aluminum. A layout and photographs of the pump stage are presented in Fig. 1.

The layout of the experimental test rig is depicted in Fig. 2. As can be observed, the setup is essentially composed of a water flow line with a tank, a booster pump, some valves and instruments to measure the impeller rotation speed (Ω), water temperature (T), pressure in the prototype inlet (P), pressure increment generated by the prototype (DP), and water flow rate (Q_W). The analog output signals from these instruments are acquired through a *National Instruments* system and the measured data is monitored and stored by a *LabVIEW* supervisory control program. The pressure transducers are mounted at the pump inlet and outlet, and the impeller rotation speed is controlled by a variable frequency drive system. The flow rate through the impeller is adjusted by setting the rotational speed of the booster pump and the opening or closing of the discharge valve assembled at the pump outlet. All instruments present uncertainties lower than 0.5% of the measured values.

Table 1: Impeller geometry

Parameter	Symbol	Value
Inlet diameter [mm]	d_1	44
Outlet diameter [mm]	d_2	110
Outlet angle of blade [$\circ$]	β_2	46.8
Blade thickness [mm]	e	5.5
Blade height [mm]	h	6.0

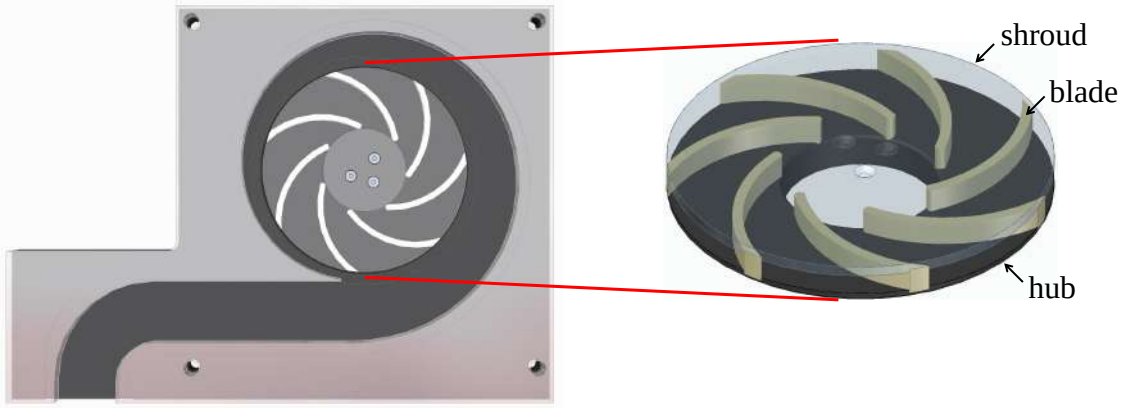

(a) Drawings of the pump stage highlighting the impeller

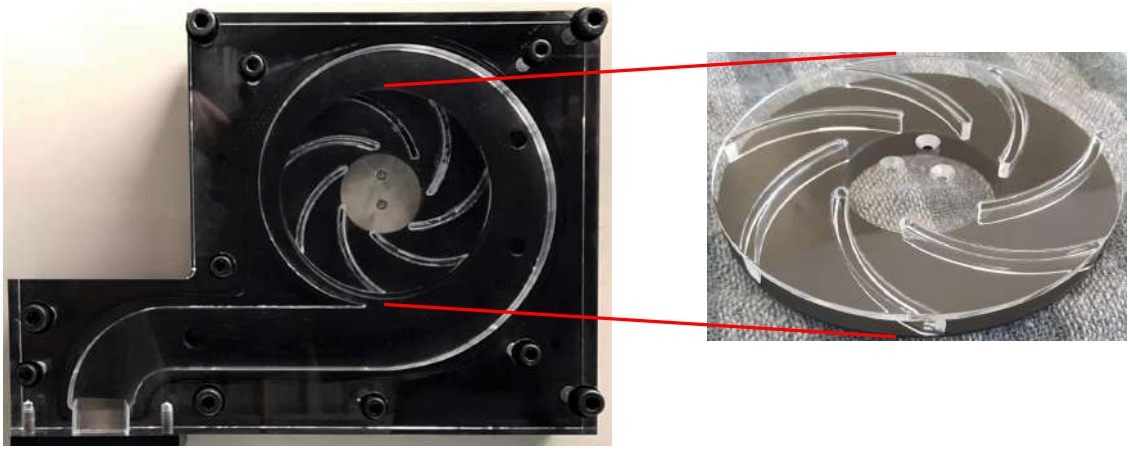

(b) Photographs of the pump stage, highlighting the impeller

Figure 1: Test pump design.

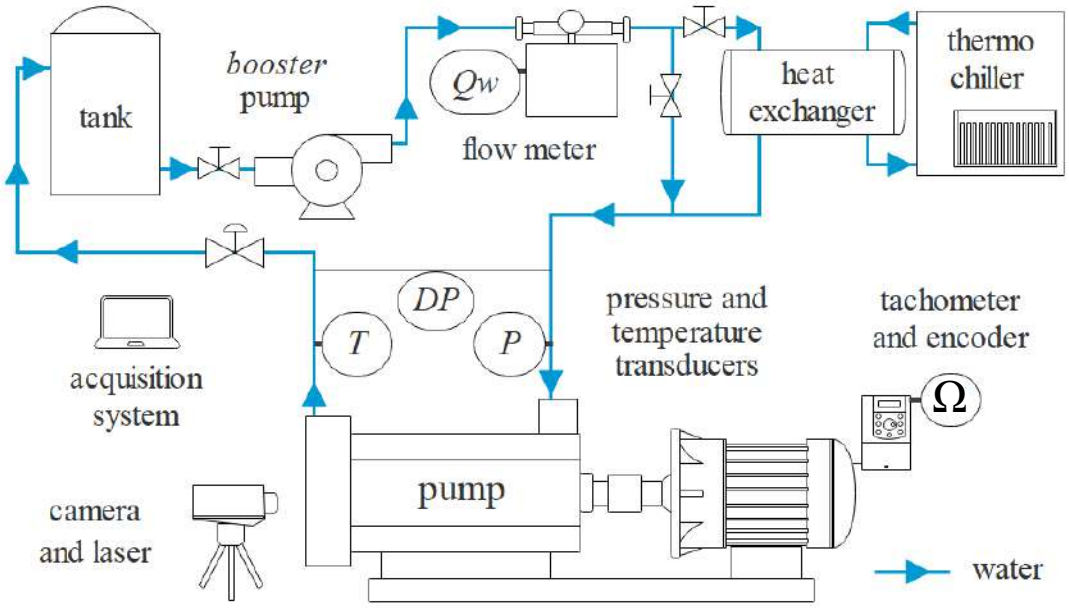

Figure 2: Layout of the experimental test rig.

2.2. PIV setup

A *DualPower 30-1000* time-resolved PIV (TR-PIV) system from *Dantec Dynamics Inc.* was used as the flow visualization method in the determination of velocity fields in the centrifugal pump impeller. The main components of the system are a power supply, a pulsed laser generator, a synchronizer, a high-speed camera (*Phantom VEO640*) and the *DynamicStudio* software which controls the PIV measurements. The system is capable of working at pulse frequencies up to 1000 Hz to provide instantaneous velocity vectors with two components in two-dimensional planes (2D2C-PIV).

The pump prototype is illuminated from both sides laterally by a dual light guide system composed of lenses and mirrors that adjust the position and thickness of the laser sheets. The mid-plane of the impeller, perpendicular to the pump shaft, was selected for the measurements. In the tests, the field-of-view covered the entire transparent stage to reveal the overview of flow structures. Fluorescent particles of PMMA doped with rhodamine-B dye were added to the water to serve as fluorescent tracers in the laser induced fluorescence (LIF-PIV) technique. These particles have an average diameter in the range from 20 μm to 50 μm.

The flow is illuminated by a double-pulsed laser (Nd:YAG type) with a wavelength of 532 nm and the flow images are captured by a high-speed camera (CMOS sensor) with a spatial resolution of 2560 px × 1600 px, the acquired images presenting a 0.1 mm/px relation. To assemble the 2D2C-PIV setup, the camera was installed perpendicular to the light sheets. A high band-pass filter for wavelengths above 545 nm was mounted on the camera lens to filter all the light scattered by the interfaces, capturing only the light fluoresced by the seeding particles. The configuration of the illumination is available in Fig. 3.

Examples of images captured during the PIV tests are shown in Fig. 4. It is evident that there is no significant image distortion, reflection or noise in the raw image (Fig. 4a). Once the experiments are completed, a pre-processing procedure is performed in the *DynamicStudio* software and an image processing algorithm, developed in MatLab®, is applied to mask out the impeller blades and volute regions in the raw images (Fig. 4b) before sending them to the PIV cross-correlation software. The Adaptive PIV method [48] with initial and final interrogation regions of 32 and 16 px, respectively, was chosen in the present study. A Gaussian fitting was used in the correlation peak to obtain accurate sub-pixel displacements. In addition, a procedure to remove the angular displacement of the impeller (in order to define a non-inertial rotating frame of reference) was implemented based on the work of Liu et al. [49]. By employing these above-mentioned processes, consistent PIV measurements have been obtained. More information on the PIV setting and image processing are available in Perissinotto et al. [43].

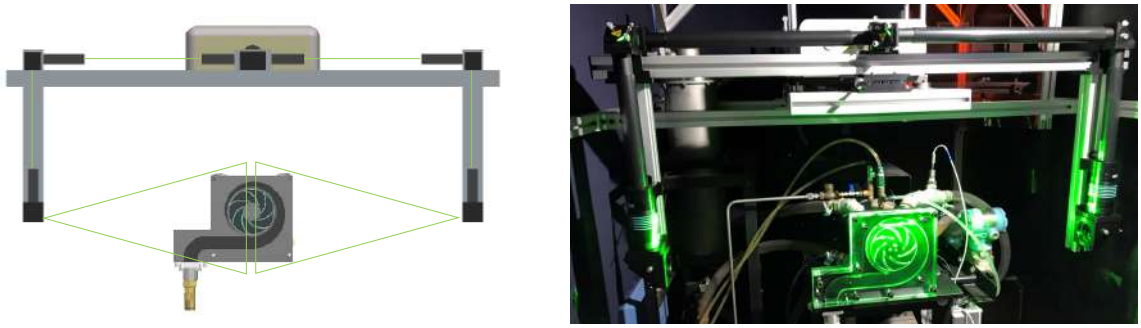

(a) Scheme of the dual light guide system

(b) Photograph of the dual light guide system

Figure 3: Experimental facility highlighting PIV system and transparent pump.

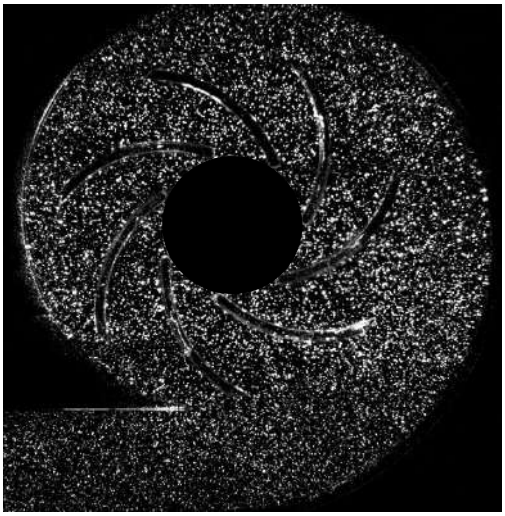

(a) PIV image before pre-processing

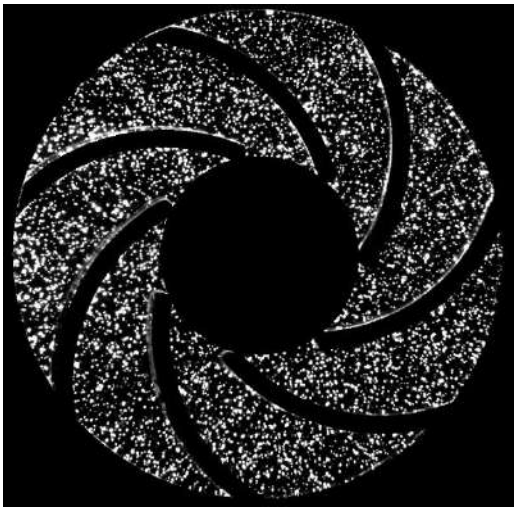

(b) PIV image after pre-processing

Figure 4: Typical PIV images acquired during the tests.

2.3. Test matrix

In the present work, PIV acquisitions were performed at three fixed rotational speeds (Ω) and three water flow rates (Q_W) for each Ω. The water flow rate is given in terms of the pump's best efficiency point (Q_{BEP}), represented by the variable Q^*. The experimental matrix is shown in Tab. 2.

Table 2: Test matrix of the experiments

Ω [rpm]	Q_W [m^3/h]	$Q^* = Q_W/Q_{BEP}$
300	0.225	0.3
	0.75	1.0
	1.125	1.5
600	0.45	0.3
	1.5	1.0
	2.25	1.5
900	0.66	0.3
	2.2	1.0
	3.33	1.5

The experimental conditions encompassed a range of Ω set at 300, 600, and 900 rpm along with nine distinct flow rates. Flow rates were quantified using a Coriolis flow meter, primarily capturing mass flow rates ($\dot{m}$), which were subsequently converted into volumetric flow rates ($Q_W = \dot{m}/\rho$). It is worth noting that throughout the experiments, the water remained at a constant temperature of T = 25°C, with corresponding fluid density of $\rho = 997$ kg/m^3. Additionally, the dynamic viscosity of the fluid at this temperature was approximated as $\mu = 0.0009$ Pa·s.

The specified flow rates adopted in the experimental matrix (Tab. 2) were determined via preliminary assessments designed to characterize the pump's operational performance. The initial computation of pump head (H_{pump}) and efficiency ($e_{ff,pump}$) was derived from instrument measurements. Subsequently, the flow rate corresponding to BEP was determined for all rotational speeds. Figure 5 illustrates the range of flow rates examined in this research, spanning from a condition near pump shut-off (with higher pump head and lower flow rate) to a condition resembling open flow (with lower pump head and higher flow rate).

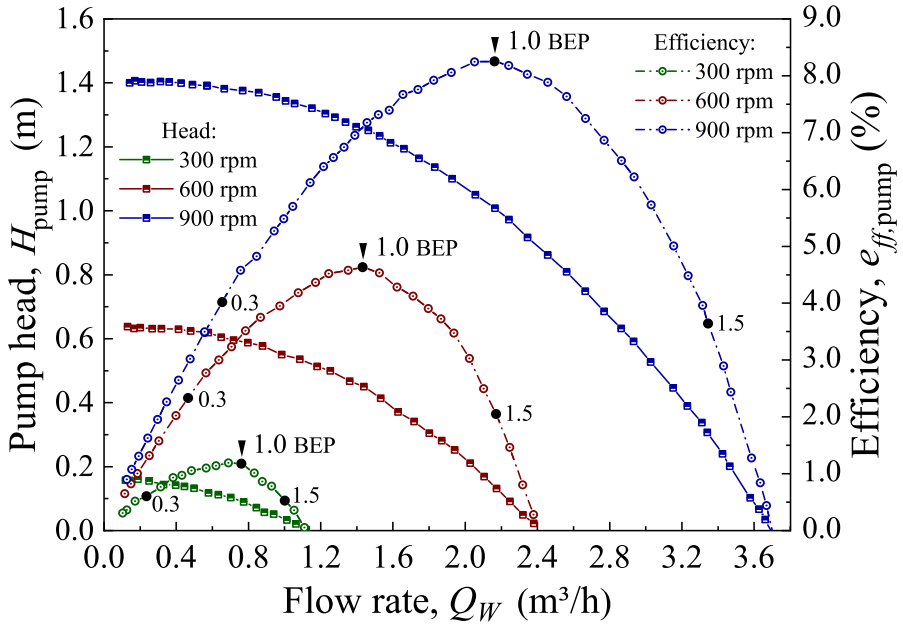

Figure 5: Performance curves of the pump prototype.

As depicted in Fig. 5, the pump exhibits an efficiency range of approximately 1% to 8% across the investigated rotational speeds, which are notably lower in comparison to typical commercial pumps. The diminished efficiency, denoted as $e_{ff,pump}$, can be attributed to frictional losses

occurring within the mechanical components situated in the transmission system of the motor-pump assembly, as detailed in Perissinotto et al. [43]. The pump assembly incorporates five bearings and three mechanical seals, each contributing to energy dissipation through friction. The total torque required to mobilize all these elements is quantified using a torque meter. Notably, the central shaft's length (approximately 80 cm) is nearly eight times greater than the diameter of the impeller (approximately 10 cm).

However, it is essential to emphasize that the relatively low efficiency of the prototype does not hinder the objectives of this study. The pump was originally designed for flow visualization purposes, and the incorporation of bearings and seals on the shaft, while diminishing efficiency, does not compromise the functionality of the apparatus. As a result, the machine continues to yield manometric curves consistent with those of a genuine centrifugal pump.

A total of 2000 pairs of pump flow images were captured in each experimental condition. The double frame TR-PIV acquisitions were conducted with a frequency of 700 Hz, while the time difference between the two consecutive frames for velocity measurement ΔT_{PIV} followed the guidelines discussed in Raffel et al. [50].

3. Proper orthogonal decomposition

Turbulent flows are composed of a wide range of temporal and spatial scales and identifying the existence of coherent structures may be a complex task. The proper orthogonal decomposition (POD) offers a way of carrying out the spatio-temporal analysis of turbulent flows, where the turbulent structures are ranked according to their energy levels. The basic idea is that structures with higher energy (usually large-scale structures) contain the main characteristics of the turbulent flow. In this section, a brief discussion on the main features of POD will be provided. Further details and mathematical formulation can be found in [51, 52].

In a turbulence analysis, the velocity vector $\mathbf{U}(\mathbf{x},\mathrm{t})$ is usually a function of space and time, and can be decomposed in a sum of the time averaged flow, $\langle \mathbf{U}(\mathbf{x},t) \rangle$, and the fluctuation field $\mathbf{u}(\mathbf{x},\mathrm{t})$, so that we can write:

$$\mathbf{U}(\mathbf{x},t) = \langle \mathbf{U}(\mathbf{x},t) \rangle + \mathbf{u}(\mathbf{x},t) \tag{1}$$

The idea behind the POD method is to decompose the fluctuation vector field $\mathbf{u}(\mathbf{x},\mathrm{t})$ into a set of deterministic spatial functions $\phi_i(\mathbf{x})$ modulated by time coefficients $a_i(t)$ so that,

$$\mathbf{u}(\mathbf{x},t) = \sum_{i=1}^{N} \phi_i(\mathbf{x}) a_i(t) \tag{2}$$

where $\phi_i(\mathbf{x})$ are the POD (spatial) modes, $a_i(t)$ are their time coefficients and N is the number of snapshots. The snapshots of $\mathbf{u}$ are computed at time t and the covariance matrix C_{ij} is defined as the product of a given number N of snapshots,

$$C_{ij} = \mathbf{u}^{\mathsf{T}}\mathbf{u} \tag{3}$$

$$C_{ij}\mathbf{A}_i = \lambda_i \mathbf{A}_i \tag{4}$$

where eigenvalues and eigenvectors of covariant matrix C_{ij} are λ_i ($\lambda_1 \geq \lambda_2 \geq \ldots \lambda_n \geq 0$) and $\mathbf{A}_i$ $[(\mathbf{A}_1, \mathbf{A}_2, \ldots, \mathbf{A}_n)]$. Based on this, the eigenvector of covariant matrix is used for projection to get POD modes under the corresponding eigenvalues of flow field as follows:

$$\phi_i = \frac{\sum_{i=1}^{N} \mathbf{A}_i \mathbf{u}_i}{\| \sum_{i=1}^{N} \mathbf{A}_i \mathbf{u}_i \|} \tag{5}$$

The transient flow field is projected onto the POD mode, and the time coefficients a_i, (Eq. 6), of each mode are obtained to characterize the spatial–temporal evolution characteristics:

$$a_i = \phi_i^{\mathsf{T}}\mathbf{u} \tag{6}$$

In this work, the spatial modes as well as the temporal coefficient are numerically obtained through Eqs. (5) and (6). An in-house code was developed in Python$^{\mathrm{TM}}$, based on Weiss [53]. The code reads the PIV instantaneous velocity fields and performs the modal decomposition of the flow using the POD snapshot technique [24]. The code is based on the numerical packages `scipy` [54] and `numpy` [55], and is available for download at `http://gitlab.com/rafacerq/snapshot-POD`, together with post-processing scripts and experimental data from this work.

4. Results and discussion

4.1. Fields of phase-ensemble averaged velocity

To investigate flow patterns within the centrifugal pump impeller, the instantaneous fields of absolute velocity were averaged through a phase-ensemble procedure. In this procedure, acquisitions are only performed when the impeller reaches a certain angular position (θ) during its

rotational motion. Therefore, when observing the images, the observer notices that the channels and blades are always in the same position. In this work, the results presented for average flow fields are positioned at $\theta = 10°$, with the reference position $\theta = 0°$ corresponding to the angle at which the tip of one of the lowest blades is vertically aligned with the tip of the volute tongue. This position was calculated using a rotary encoder (see Fig. 2). The phase-ensemble averaged absolute velocity was determined using Eq. (7):

$$\langle \mathbf{U} \rangle = \frac{1}{N} \sum_{i=1}^{N} \langle \mathbf{U}_i \rangle \tag{7}$$

The relative velocity was obtained by subtracting the absolute velocity from the tangential term due to the impeller motion in the velocity triangle [56]:

$$\langle \mathbf{W} \rangle = \langle \mathbf{U} \rangle - \omega \mathbf{r} \tag{8}$$

where ω represents the angular speed, proportional to the rotational speed Ω, and $\mathbf{r}$ is the radial position of the velocity vector in relation to the impeller center.

The results of the fields of phase-ensemble averages of the relative velocity and streamline plots are shown in Fig. 6 for fixed pump impeller rotational speeds (Ω) of 300, 600 and 900 rpm under the different flow rates (Q^*) of 0.3, 1.0 and 1.5. The impeller rotation direction is clockwise, and the relative velocities presented have been normalized by the blade tip speed $\langle W^* \rangle = \langle W \rangle / U_{tip}$ [10].

As can be seen from Figs. 6b, 6e and 6h, at the BEP ($Q^* = 1.0$) the streamlines follow the curvature of the blades without significant flow separation for the three investigated rotational speeds. Low velocity zones develop on the pressure sides of the blades, generating an pressure gradient, which suggests that the fluid is displaced towards the suction sides. As a consequence, we observe the "jet-wake" phenomenon in the suction blades of all impeller channels. Furthermore, due to the blade curvature, the flow near the impeller center is dominated by rotational effects. As the fluid moves towards larger radii, the Coriolis force increases and the fluid is pushed in the opposite direction, towards the pressure side. As a result of this phenomenon, we can identify very uniform velocity fields in the impeller exit region.

As the flow rate decreases to $Q^* = 0.3$ (Figs. 6a, 6d and 6g), the fluid near the suction blade is diverted to the pressure blade causing a change in the stagnation point, as a consequence of the unbalance of apparent forces. Then, a significant reduction in the velocity is detected, resulting in

recirculation zones next to the suction blades. We observe that this vortex generation mechanism is closely linked to regions where the fluid outlet area is reduced by the solid walls in the volute spiral, especially on the left side of the pump stage, in the channels 1, 6 and 7, as indicated in Fig. 6a.

As the flow rate increases to $Q^* = 1.5$ (Figs. 6c, 6f and 6i), the formation of small flow instabilities is detected on the pressure side of the blades in different radial positions of the impeller, which is probably due to the detachment of the boundary layer caused by an adverse pressure gradient. In addition, the presence of intense jets on the suction blades is also observed, as the streamlines are distorted and acquire a shape comparable to half a counter-clockwise vortex.

Another important information from the fields presented in Fig. 6 is that for two identical flow rates (normalized by the BEP Q^*), the morphology of the flow field in the impeller tends to be similar, independently of the rotational speed (Ω) and absolute flow rate (Q_W). In other words, the average flow field follows the affinity laws of centrifugal pumps. This result agrees with the observations made by Perissinotto et al. [43].

4.2. Phase-ensemble averaged turbulent kinetic energy fields

The turbulent kinetic energy is of particular interest for analyses of the total energy distribution of the flow field. Since only two components of the velocity fluctuations are available in our 2D2C-PIV measurements, an isotropic assumption is applied when calculating the turbulent kinetic energy, K_{2D},

$$K_{2D} = \frac{1}{2}\langle \mathbf{u} \cdot \mathbf{u} \rangle \tag{9}$$

The results for the phase-ensemble averaged turbulent kinetic energy are presented in Fig. 6 normalized by the blade tip velocity $K^*_{2D} = K_{2D}/U^2_{tip}$. Figure 7 reveals that the highest turbulence values are detected at the lowest flow rate condition, $Q^* = 0.3$ (Fig. 7a, 7d and 7g), especially near the impeller exit. This fact occurs because when the fluid flows through the impeller, not only rotational energy is provided to it, but also the volute itself imposes a geometric restriction. Thus, the highest values of K^*_{2D} are located at the leftmost impeller, in channels 1, 6 and 7, which are close to regions where the volute radius is small. Exiting the impeller, the fluid impinges the volute wall and suddenly changes its direction, this fact resulting in the formation of recirculation zones in the impeller channels. In addition, the flow exiting the impeller in channels 1 and 2 is affected by the presence of the volute tongue. In this region, as the fluid exits the impeller, it

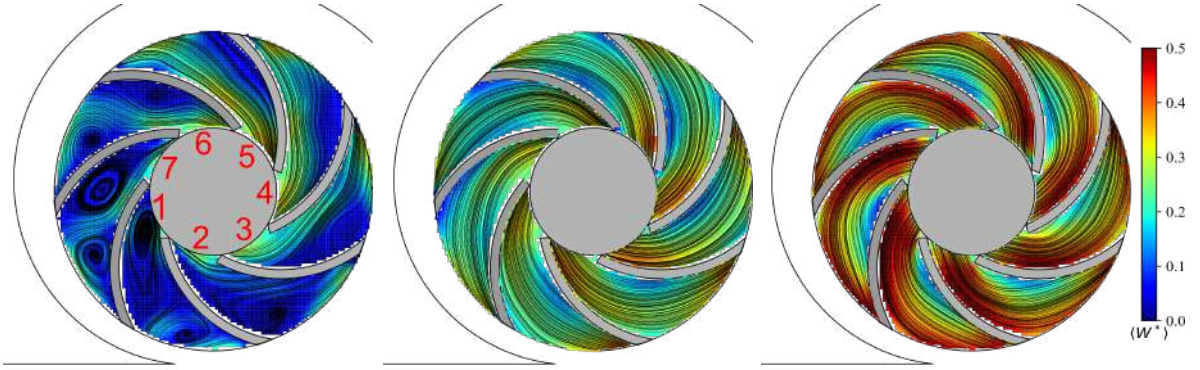

(a) $Q^* = 0.3$ - 300 rpm (b) $Q^* = 1.0$ - 300 rpm (c) $Q^* = 1.5$ - 300 rpm

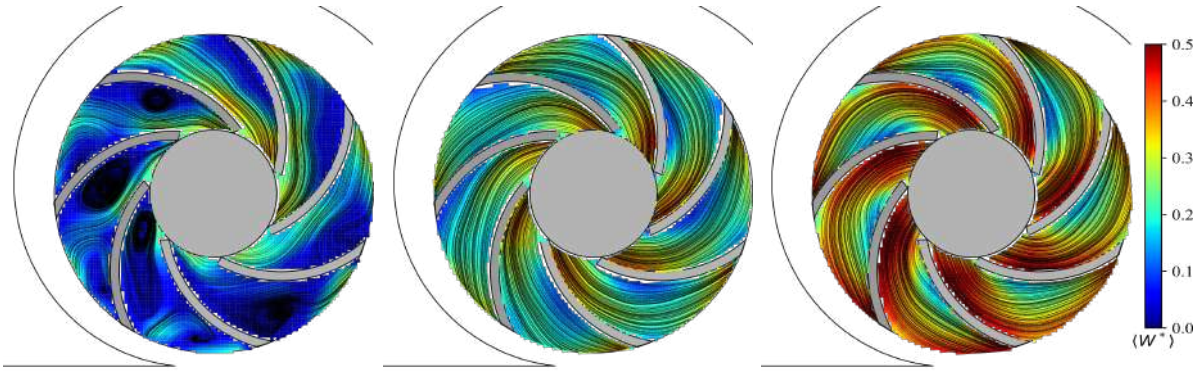

(d) $Q^* = 0.3$ - 600 rpm (e) $Q^* = 1.0$ - 600 rpm (f) $Q^* = 1.5$ - 600 rpm

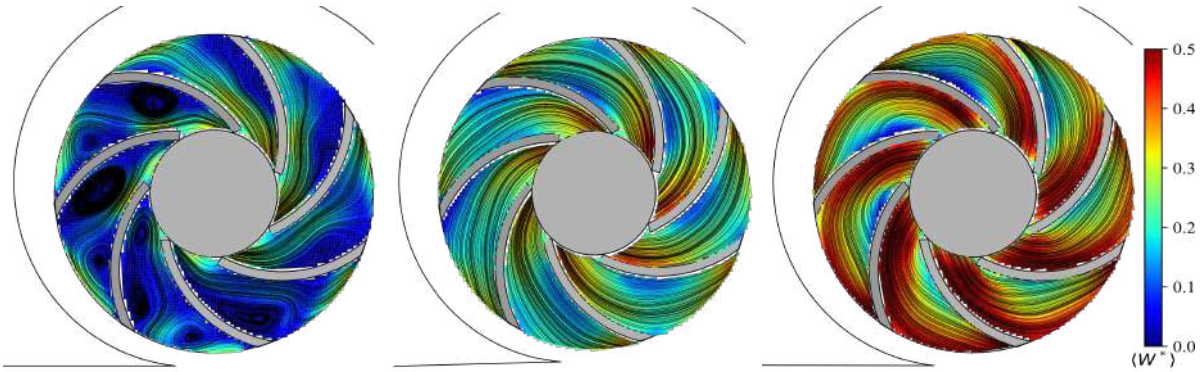

(g) $Q^* = 0.3$ - 900 rpm (h) $Q^* = 1.0$ - 900 rpm (i) $Q^* = 1.5$ - 900 rpm

Figure 6: Streamlines from ensemble-average velocity field in the centrifugal pump impeller.

faces a sudden change of direction due to the sharp surface of the tongue tip, which promotes recirculation. Those two effects combined result locally in regions with intense turbulent kinetic energy.

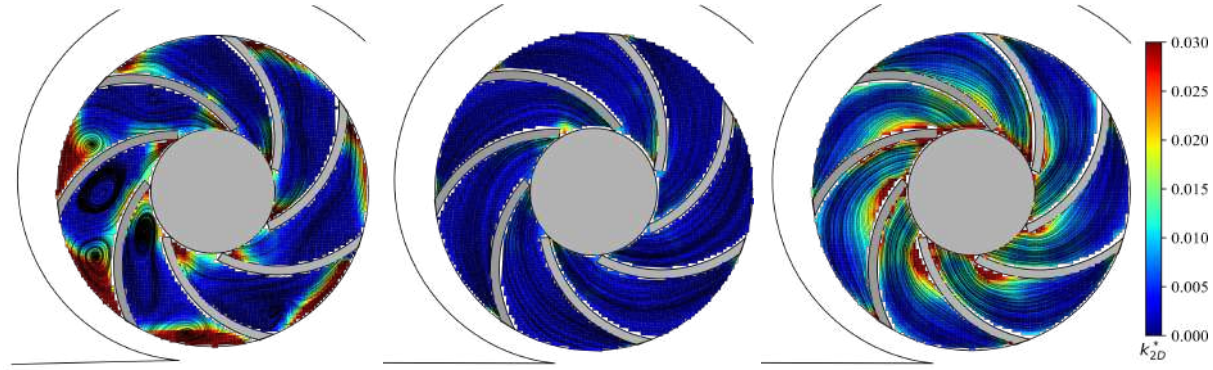

(a) $Q^* = 0.3$ - 300 rpm (b) $Q^* = 1.0$ - 300 rpm (c) $Q^* = 1.5$ - 300 rpm

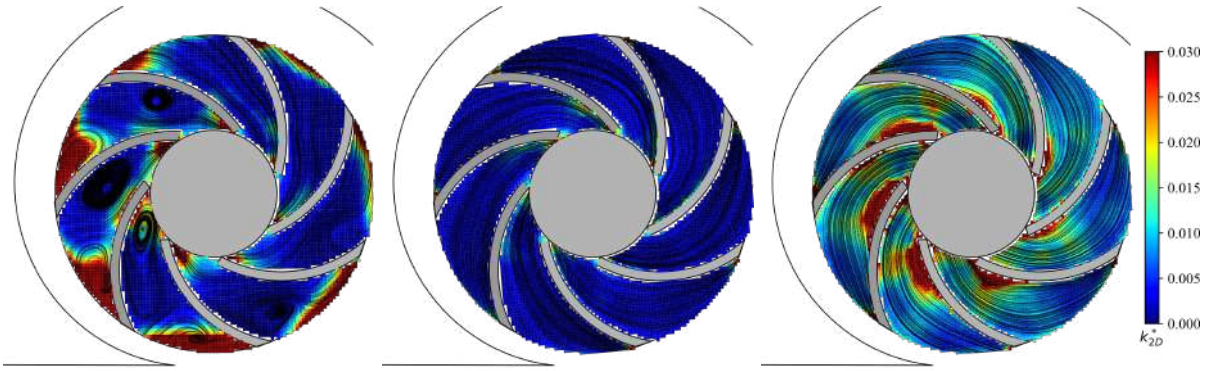

(d) $Q^* = 0.3$ - 600 rpm (e) $Q^* = 1.0$ - 600 rpm (f) $Q^* = 1.5$ - 600 rpm

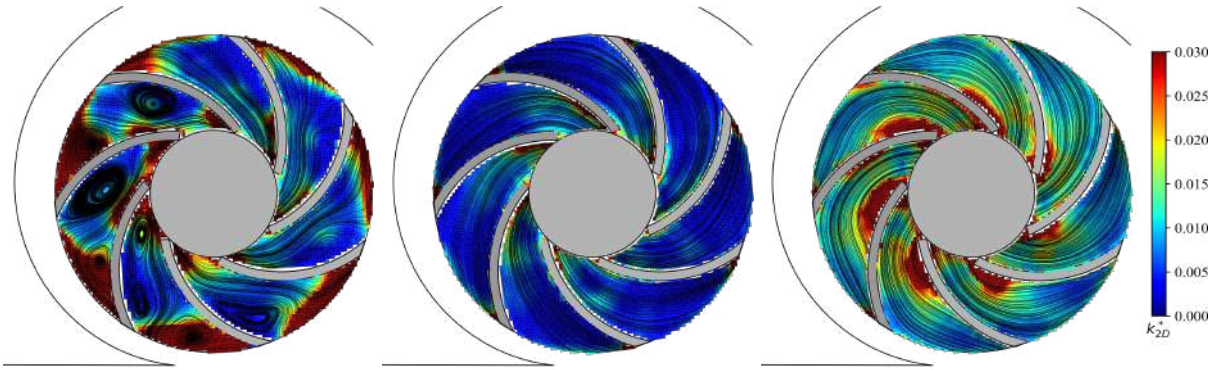

(g) $Q^* = 0.3$ - 900 rpm (h) $Q^* = 1.0$ - 900 rpm (i) $Q^* = 1.5$ - 900 rpm

Figure 7: Streamlines from the fields of ensemble-average turbulent kinetic energy in the centrifugal pump impeller.

In opposition, for the design condition ($Q^* = 1.0$ Figs. 7b, 7e and 7h) the turbulence production has much lower values. The limited K^*_{2D} values are associated with the uniformity of the flow field, since centrifugal pumps working at the BEP tend to have well-organized velocity fields without

flow detachment zones. This is a consequence of well-balanced forces governing the fluid behavior in the impeller at the design point.

For higher flow conditions (such as $Q^* = 1.5$, Figs. 7c, 7f and 7i) we observe that regions with high values of turbulent kinetic energy are found near the pressure surfaces of the blades. As discussed in section 4.1, these regions are characterized by low average velocities, which suggests the occurrence of flow detachment events. Therefore, the turbulence production in the centrifugal pump impeller is attributed to the geometric restrictions imposed by the volute walls, as well as the unbalance of apparent forces, which would be responsible for the formation of vortices and for the instabilities in the regions next to the boundary layer of the blades.

4.3. POD analysis

Physical quantities of turbulent flows can be divided into time-averaged and fluctuation quantities, the latter consisting of periodic random parts. The periodic part represents the large-scale coherent structures, while the random part represents the small-scale turbulence [57]. The POD method is as an effective tool to identify the fluctuation part, in which two key quantities are obtained: the eigenvalues (λ_i) and the modes (ϕ_i). The modes represent different structures of the flow field, and the eigenvalues are related to the flow field energy.

4.3.1. Distribution of flow energy

Figure 8 shows the distribution of the turbulent kinetic energy ($\lambda_n / \sum_{i=1}^{N} \lambda_i$) associated with individual modes of the eigenvalues spectrum (LHS), and the cumulative energy ($\sum_{i=1}^{n} \lambda_n / \sum_{i=1}^{N} \lambda_i$, on the RHS) for the various rotational speeds and flow rates in the pump impeller. For the lowest flow rate ($Q^* = 0.3$), 40 to 50% of the turbulent energy of the flow is concentrated in the first and second POD modes for the three Ω investigated here. For the design condition ($Q^* = 1.0$), the first two modes are responsible for 10% of the turbulent energy, with 60 modes being necessary to reach 50% of the total energy. Finally, for the highest flow rate ($Q^* = 1.5$), 20%, 9% and 12% of the cumulative energy are contained in the first two modes at rotation speeds of 300, 600 and 900 rpm, respectively. These distributions of energy level indicate that there is a significant redistribution to POD modes for different flow rates. However, the distribution of turbulent kinetic energy for a same flow rate in relation to the BEP is approximately the same for the different rotational speeds imposed on the impeller.

The rapid decrease in the energy levels for $Q^* = 0.3$ indicates that the first two modes may contain large-scale coherent structures of turbulent fields. Looking at the first few modes for this

condition would be sufficient to identify dominant coherent motions. Furthermore, the third and fourth modes, which contain less energy, would represent the small-scale flow structure. As the modes continue to increase, the energy level changes little, so that it can be understood that the higher-order modes represent random fluctuations and noise in the turbulent field.

For the design ($Q^* = 1.0$) and higher ($Q^* = 1.5$) flow rates, the large-scale and coherent flow structures become more incoherent and smaller. This suggests that the large-scale structures (with higher energy) are broken into small-scale structures (with lower energy), in a process known in turbulence theory as cascade effect [58].

As mentioned above, the distribution of turbulent energy is approximately independent of the pump rotation speed, being a function only of the flow rate. This observation is confirmed in Figs. 6 and 7, where we can see that the flow topology is very similar for 300, 600 and 900 rpm. Hence, the next sections will focus only on the intermediate rotational speed $\Omega = 600$ rpm, while other rotations will be suppressed since they do not add new information to the discussions. Nevertheless, the analysis was performed for 300 rpm and 900 rpm as well, and we noticed that the results are roughly the same.

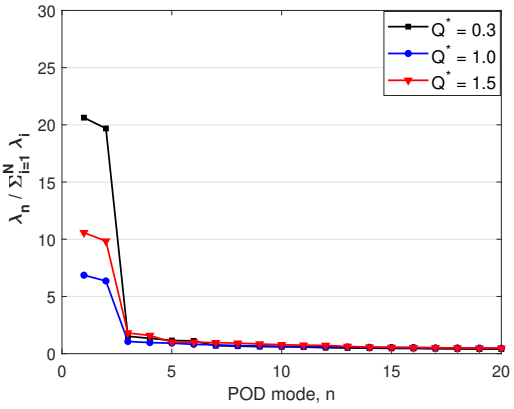

(a) Normalized energy of individual modes - 300 rpm

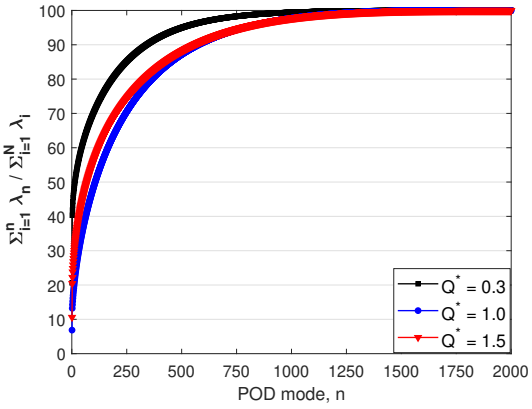

(b) Cumulative energy of the modes - 300 rpm

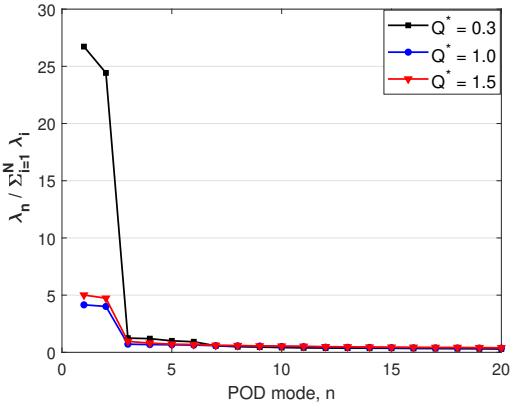

(c) Normalized energy of individual modes - 600 rpm

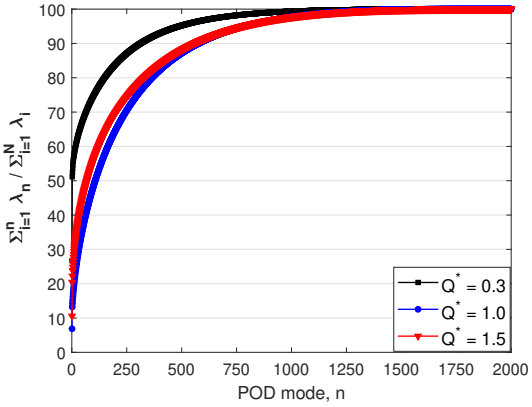

(d) Cumulative energy of the modes - 600 rpm

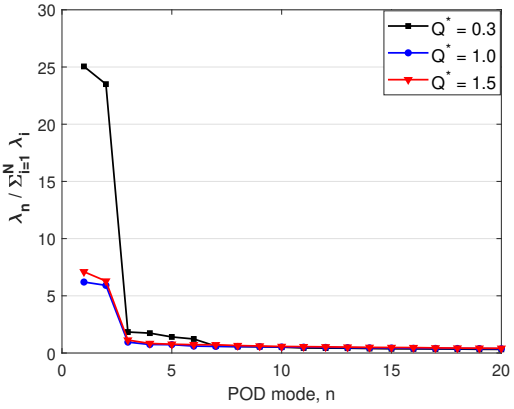

(e) Normalized energy of individual modes - 900 rpm

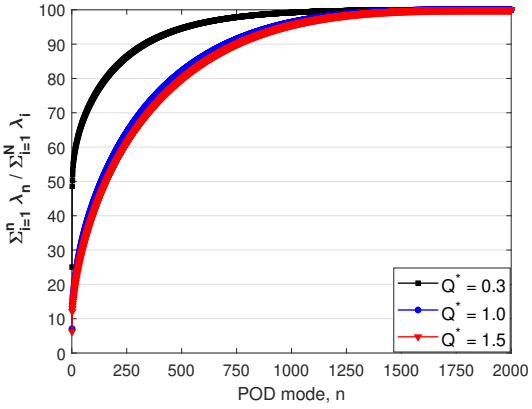

(f) Cumulative energy of the modes - 900 rpm

Figure 8: Energy distribution in the centrifugal pump impeller.

4.3.2. Spatial characteristics

The spatial distribution of the first two POD modes is shown in Fig. 9, for the three studied flow rates, at the rotation speed of 600 rpm. It can be observed that there is a coupling between the first two modes, their spatial distribution revealing that these modes occur in pairs. Indeed, when comparing Fig. 9a with Fig. 9b, Fig. 9c with Fig. 9d, and Fig. 9e with Fig. 9f, we notice that the structure of both modes is the same, except for a shift in the phase, as if mode 2 was rotated a certain angle relative to mode 1. This fact will be discussed in section 4.3.3.

At the lowest flow rate ($Q^* = 0.3$), we observe regions with more intense reddish tones, where vortices or flow separation are found (Fig. 9a and 9b). This means that the velocity fluctuations in these regions tend to be correlated. From Fig. 6, we can see that the streamlines for this condition are completely misaligned in relation to the blades curvature, and, when analyzing regions far from the volute tongue, we notice that the flow that tends to separate. In the region near the volute tongue, large-scale vortices develop and rotate in the opposite direction with respect to the impeller motion, which is a effect resulting from the direct flow (related to the flow rate) and the counter-rotating flow (resulting from the fluid tending to keep its angular momentum, as discussed in Zhang et al. [8]). These unsteady flow structures are detected by the POD method as coherent structures with a high energy level.

For the design condition ($Q^* = 1.0$), Fig. 6 revealed smooth streamlines and "jet-wake" zones. When analyzing the POD modes (Figs. 9c and 9d), we can observe that the velocity fluctuations for such a condition tend to be more correlated in regions where "jet-wakes" are present. However, these fluctuations are less correlated in comparison with those found at the lowest flow rate. As already discussed in section 4.3.1, this is an indication that a large-scale flow with high energy is breaking into small-scale flow structures.

As the flow rate increases to $Q^* = 1.5$, we can see in Fig. 8 that the average values of the first two POD modes are approximately equal to those presented for $Q^* = 1.0$. These results are associated with the flow structures shown in Figs. 6 and 7. At the BEP condition, the streamlines are smooth and aligned with the curvature of the blades, so that the velocity fluctuations are very low. For $Q^* = 1.5$, however, the streamlines become inclined in the vicinity of the pressure blades, which generates velocity fluctuations interpreted here as a detachment of the boundary layer. These detaching streamlines are a consequence of small instabilities, which are characterized by structures of lower energy, represented in Figs. 9e and 9f as yellow and orange colors. The analysis is repeated for modes 3 and 4 in Fig. 10, for the same pump operating conditions.

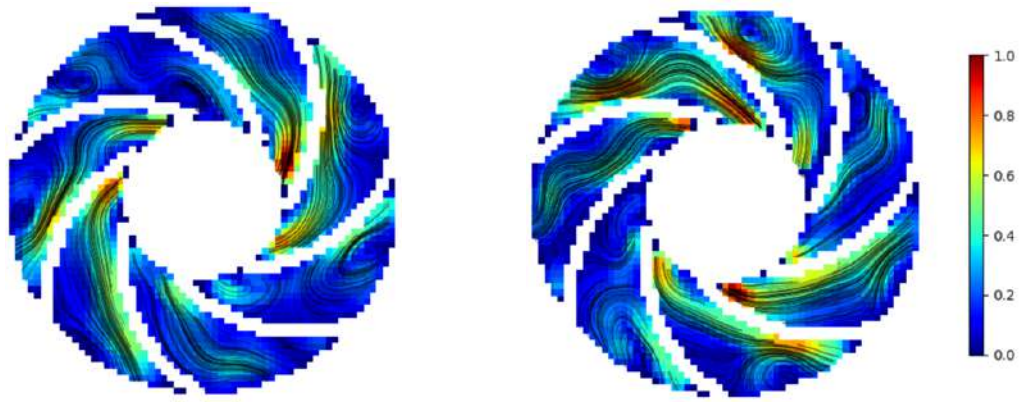

(a) Mode 1 - $Q^* = 0.3$

(b) Mode 2 - $Q^* = 0.3$

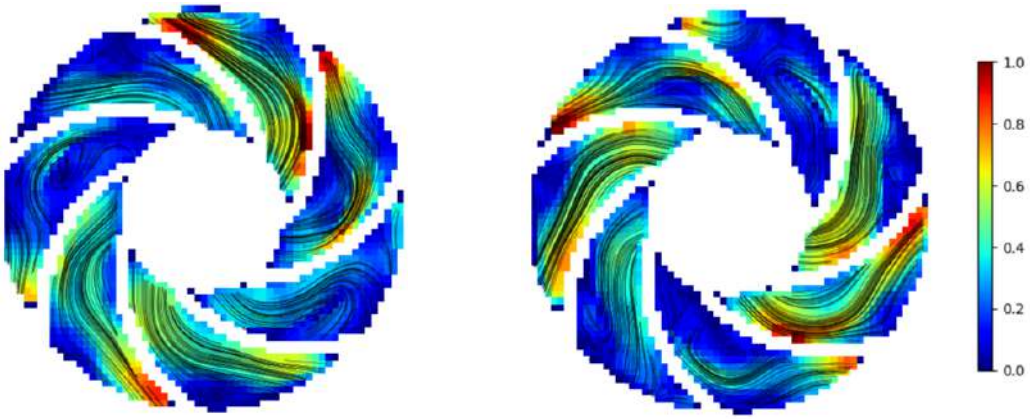

(c) Mode 1 - $Q^* = 1.0$

(d) Mode 2 - $Q^* = 1.0$

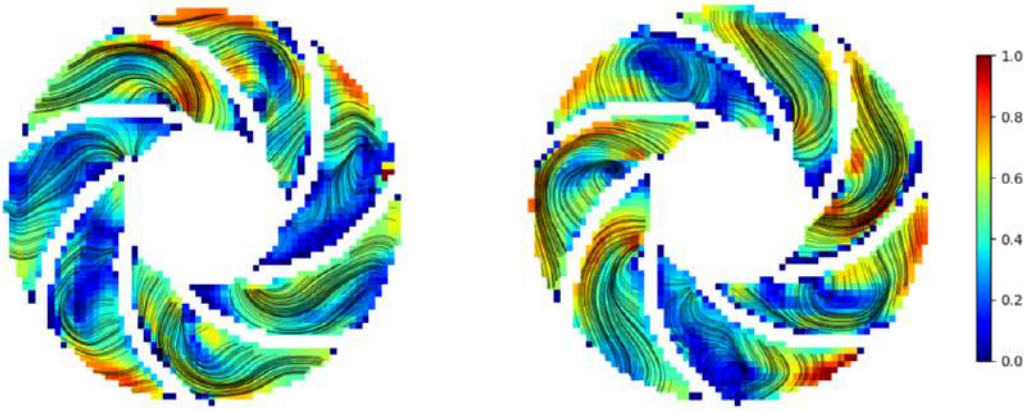

(e) Mode 1 - $Q^* = 1.5$

(f) Mode 2 - $Q^* = 1.5$

Figure 9: Spatial distribution of the first and second modes at 600 rpm for different flow rates.

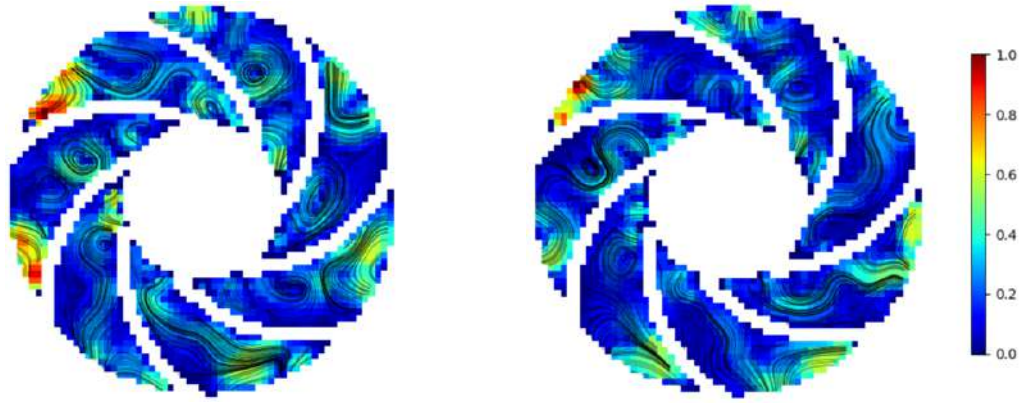

(a) Mode 3 - $Q^* = 0.3$

(b) Mode 4 - $Q^* = 0.3$

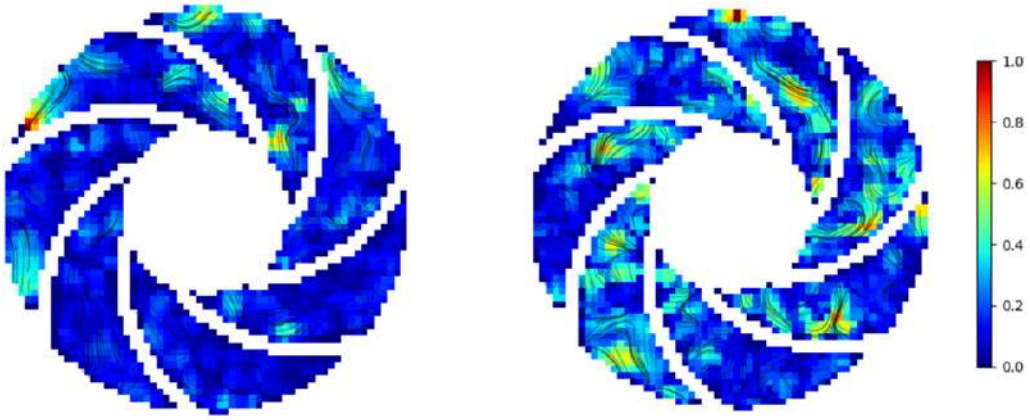

(c) Mode 3 - $Q^* = 1.0$

(d) Mode 4 - $Q^* = 1.0$

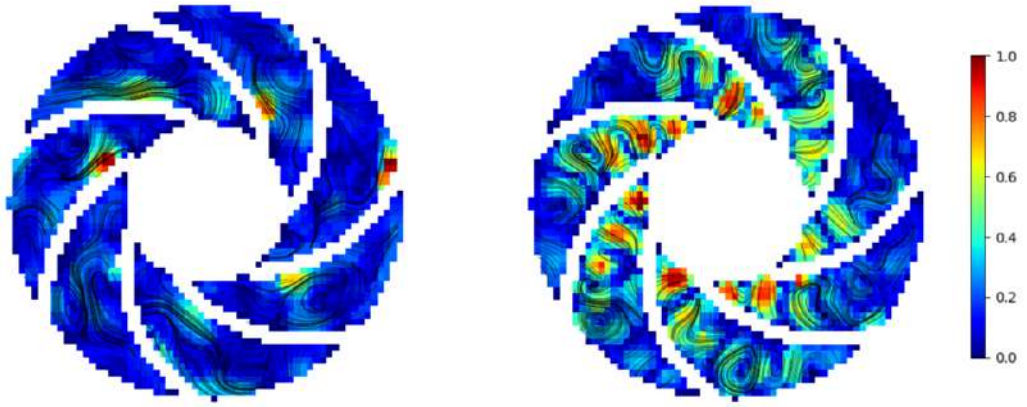

(e) Mode 3 - $Q^* = 1.5$

(f) Mode 4 - $Q^* = 1.5$

Figure 10: Spatial distribution of the third and fourth modes at 600 rpm for different flow rates.

The contours for $Q^* = 0.3$ in Fig. 10 show correlated zones of velocity fluctuation in the fluid leaving the impeller to the volute. In addition, we can also observe that modes 3 and 4 present characteristics of a vortex shedding flow pattern, process responsible for the unstable flow separation. Thus, these results indicate that modes 3 and 4, at this low flow rate, are associated with flow structures exiting the impeller as well as large-scale structures breaking into small-scale structures. Such observations are best visualized in **Video 1** of the Supplementary Material, which shows an animation of how the addition of POD modes contributes to the flow reconstruction.

For the design condition, it is more difficult to associate the higher-order modes with a physical mechanism, since all the impeller channels of the centrifugal pump have zones with a low level of correlation between velocity fluctuations. Differently, for $Q^* = 1.5$, it is possible to identify flow structures similar to those found for the lowest flow rate, but with smaller scales. From mode 4 (Fig. 10f), regions of correlated velocity fluctuations in the vicinity of the impeller eye are also detected, indicating that the instabilities responsible for the boundary layer detachment are being captured by this POD mode.

In summary, as the rank of POD modes increases, the energy of velocity fluctuations decreases for all flow conditions studied in this paper. Modes 1 and 2 are responsible for larger-scale unstable flow structures, i.e., large vortices and "jet-wakes", whereas modes 3 and 4 are associated with smaller-scale unstable structures. Above that, the addition of more POD modes does not contribute significantly to the physics of the flow, as these higher modes are related to the noise, inherent in the PIV technique (see **Video 1** of the Supplementary Material).

4.3.3. Temporal characteristics

According to the previous section, there is a coupling between the pairs of POD modes. To further investigate this observation, the temporal characteristics of modes 1-2 and 3-4 for $\Omega = 600$ rpm are determined in the present section. The temporal coefficients, frequency spectra, as well as phase diagrams between the pairs of modes are presented in Figs. 11, 12 and 13. The analysis of the temporal coefficients of the first two POD modes for the three flow conditions confirms the similarities between the structures (Fig. 11a, 11c and 11e): both show periodicity with similar amplitudes of the peaks. This is an evidence that the modes represent a periodic structure of the water flow.

At $Q^* = 0.3$, the temporal coefficients for the first two modes have the same characteristics, except for a phase shift (Fig. 11a). In addition, a well-defined peak frequency corresponding to 10

Hz is identified for both modes (Fig. 11b), this being consistent with the rotation frequency of the pump impeller (600 rpm = 10 Hz). The distinct single peak indicates that there is a single flow phenomenon described by the first two modes at this flow rate. For the design ($Q^* = 1.0$) and highest flow rate conditions ($Q^* = 1.5$), we observe the same properties as those presented for $Q^* = 0.3$, but with a lower matching level. This is a consequence of the energy present in the first two modes of each case analyzed. From Figs. 11d and 11f, it is clear that the dominant frequency of modes 1 and 2 is still the pump rotation speed.

For modes 3 and 4, the distributions of temporal coefficients indicate that there is no correlation at the flow rates analyzed in this paper (Fig. 12). However, we note that for $Q^* = 0.3$ modes 3 and 4 are the harmonics of modes 1 and 2, characterized by smaller energy spectra. These results suggest that large flow structures form at a frequency similar to the rotation speed of the pump impeller and then break up into smaller structures at a rate that corresponds to two impeller revolutions. Furthermore, for the design condition ($Q^* = 1.0$), the frequency spectra are noisy, and several peaks at relatively low amplitudes can be observed. For $Q^* = 1.5$, one peak can be seen at 20 Hz, which is also a harmonic of the first two modes. Such results again suggest that higher-order POD modes represent small-scale unstable flow structures in the centrifugal pump impeller, which are deriving from the cascade effect.

The different POD modes can also be analyzed through phase diagrams of temporal coefficients, as shown in Fig. 13. According to Semeraro et al. [39], pairs of POD modes characterized by quasi-circular phase diagrams are comparable to Fourier modes, where the phase diagrams plots are perfect circles. Thus, POD pairing can be considered a criterion to assess the similarity between POD modes.

The phase diagrams of the first two modes for $Q^* = 0.3$, $Q^* = 1.0$ and $Q^* = 1.5$ are depicted, respectively, in Figs. 13a, 13b, 13c. We observe that for such flow conditions, the trajectory exhibits an circular behavior, similar to the one observed for vortex shedding behind a cylinder [29]. Thus, it is believed that the POD modes 1 and 2 represent vortical structures in the impeller, for which large-scale structures at low flow rates break up into small-scale structures when the flow rate increases and reaches the design point. This trend is shown in Fig. 8 and also by the scale of the axes that compose the phase diagrams in Fig. 13.

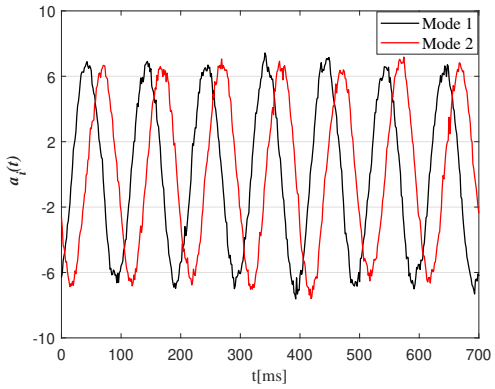

(a) Time coefficients - $Q^* = 0.3$

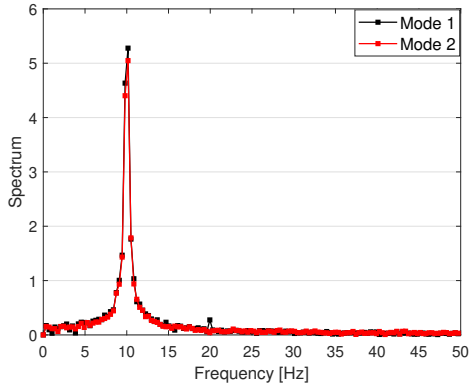

(b) FFT distribution - $Q^* = 0.3$

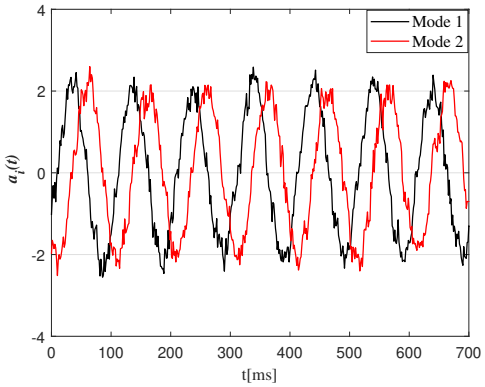

(c) Time coefficients - $Q^* = 1.0$

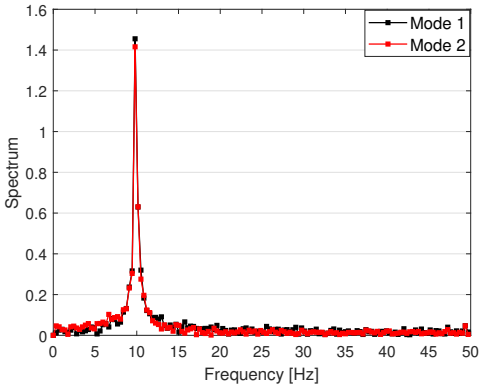

(d) FFT distribution - $Q^* = 1.0$

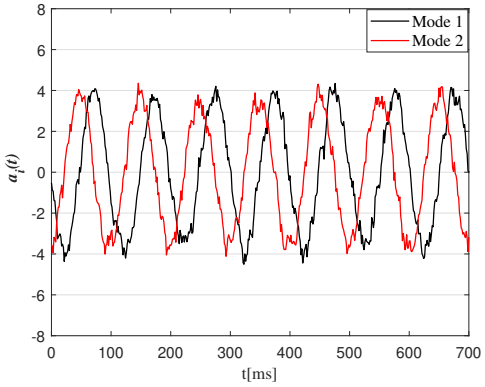

(e) Time coefficients - $Q^* = 1.5$

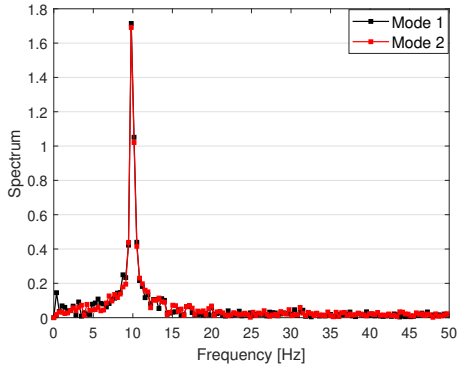

(f) FFT distribution - $Q^* = 1.5$

Figure 11: Time coefficients and FFT distribution of the first two modes at 600 rpm for different flow rates.

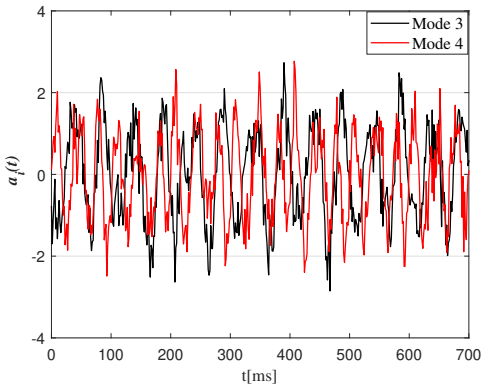

(a) Time coefficients - $Q^* = 0.3$

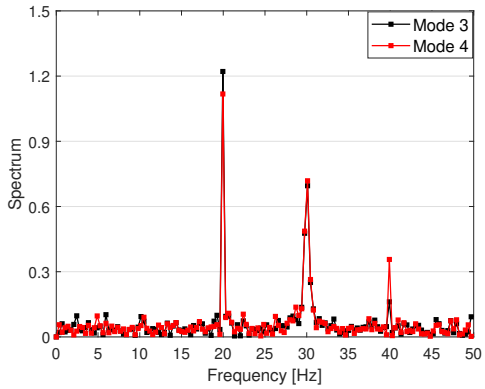

(b) FFT distribution - $Q^* = 0.3$

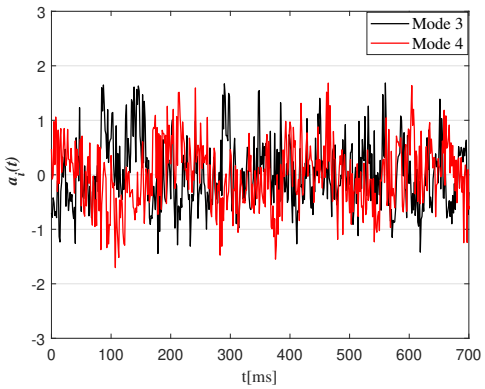

(c) Time coefficients - $Q^* = 1.0$

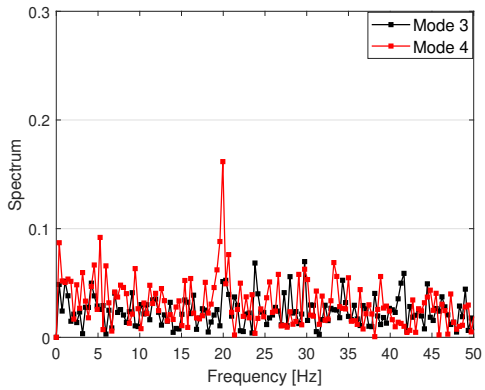

(d) FFT distribution - $Q^* = 1.0$

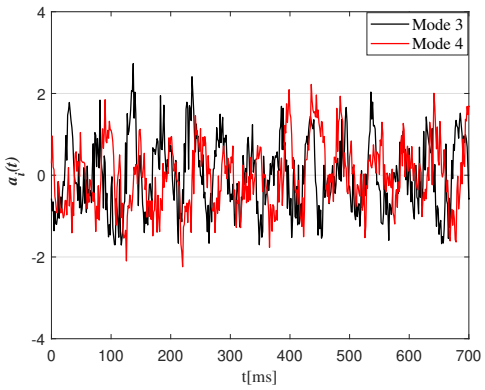

(e) Time coefficients - $Q^* = 1.5$

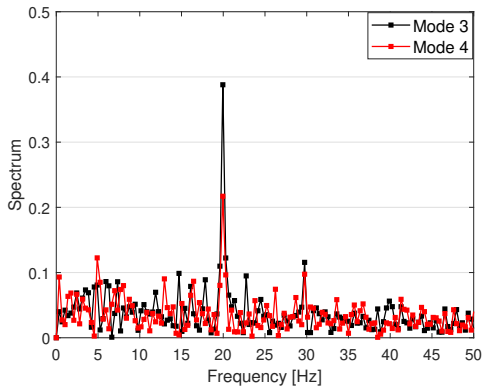

(f) FFT distribution - $Q^* = 1.5$

Figure 12: Time coefficients and FFT distribution of the third and fourth modes at 600 rpm for different flow rates.

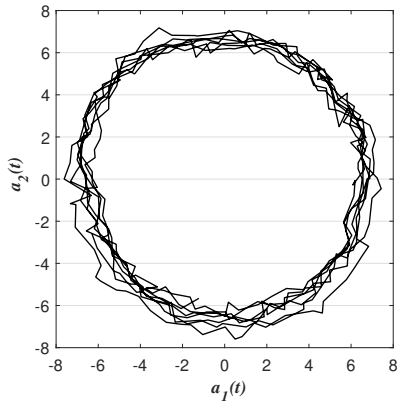

(a) $Q^* = 0.3$

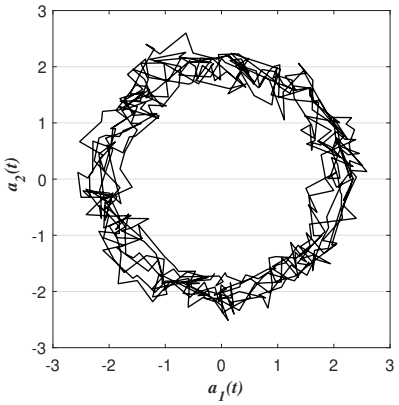

(b) $Q^* = 1.0$

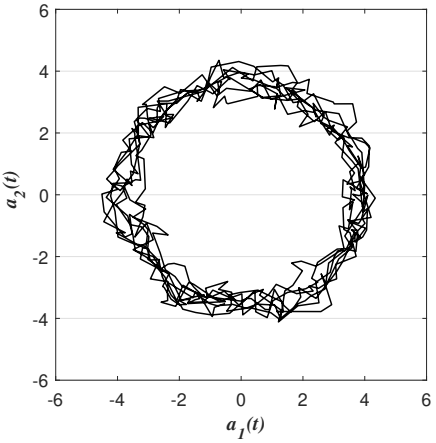

(c) $Q^* = 1.5$

Figure 13: Phase diagram of the first two modes at 600 rpm for different flow rates.

5. Conclusions

In this paper, we made use of POD of time-resolved flow fields to investigate the flow in the impeller of a centrifugal pump. For that, we carried out experiments using TR-PIV in a pump of transparent material operating at different conditions: rotational speeds of 300, 600 and 900 rpm, with water flow rates (normalized by the best efficiency point) of $Q^* = 0.3$, 1.0 and 1.5. From a detailed analysis of the flow structure, we can draw the following conclusions:

1. From the averages of relative velocities, we show that several recirculation regions develop in the impeller for a flow rate of $Q^* = 0.3$. This occurs due to a change in the stagnation point, which is a consequence of the unbalance of apparent forces at this flow condition. This flow pattern is observed for all rotation speeds investigated. At the flow corresponding to the BEP ($Q^* = 1.0$), the streamlines follow the curvature of the blades without significant flow separation for the three rotational speeds. As the flow rate increases to $Q^* = 1.5$, the formation of small instabilities is detected on the pressure side of the blades in different radial positions of the impeller, which may be associated with the detachment of the boundary layer.
2. From the turbulent kinetic energy, we show that the highest turbulence values are detected at the lowest flow rate ($Q^* = 0.3$), especially next to the impeller exit. In opposition, for the design ($Q^* = 1.0$) and highest flow rates ($Q^* = 1.5$), the turbulent kinetic energy presents lower values. This fact is a consequence of the flow uniformity, as the apparent forces are balanced for these two last conditions.
3. From the POD analyses for the low flow rate condition ($Q^* = 0.3$), the first pair of modes are correlated, and 50% of the total turbulent energy is contained in these modes. Such results suggest the occurrence of possible coherent structures for this pump operating condition, for the three rotational speeds studied in this paper. As the flow rate increases to the design point ($Q^* = 1.0$), the flow tends to be well-behaved, so that more POD modes are needed for the reconstruction of the flow. This is an indication that this condition is dominated by turbulent structures of smaller scales. The same is observed for the higher flow rate ($Q^* = 1.5$).
4. From the temporal characteristics of the flow, we conclude that the unstable flow structures with higher energy levels are formed at a frequency comparable to the pump rotation speed. Then, these structures break up at harmonic frequencies. In other words, these structures are initially coherent, but then they break up into smaller vortices through the cascade effect.

Acknowledgments

We gratefully acknowledge the support of EPIC - Energy Production Innovation Center, hosted by the University of Campinas (UNICAMP) and sponsored by FAPESP – The São Paulo Research Foundation (Process Number 2017/15736-3). We also thank FAPESP for providing the PIV system used in this research through the Multi-User Equipment program (Process Number 2019/20870-6). We acknowledge the support of ANP (Brazil's National Oil, Natural Gas and Biofuels Agency) through the R&D levy regulation. The acknowledgments are also extended to Center for Energy and Petroleum Studies (CEPETRO), School of Mechanical Engineering (FEM), and ALFA Research Group.

Declarations

Ethical approval

Not applicable. This manuscript is not related to human and/or animal studies.

Competing interests

There are no interests of a financial or personal nature.

Authors' contributions

Conceptualization: William Fonseca, Rafael Cerqueira and Erick Franklin. Original draft preparation: William Fonseca, Rafael Cerqueira and Rodolfo Perissinotto. Review and editing: William Fonseca, Rodolfo Perissinotto, Rafael Cerqueira, Erick Franklin, Marcelo Castro and William Monte Verde. Supervision: Rafael Cerqueira and Erick Franklin. Project administration: William Monte Verde. Funding acquisition: Marcelo Castro. All authors have read and agreed to the published version of the manuscript.

Funding

FAPESP – Process Numbers 2017/15736-3 and 2019/20870-6.

Availability of data and materials

If requested by the journal or the reader, the authors can provide samples of the database used to produce the results presented in this manuscript.

References

[1] R. M. Perissinotto, W. M. Verde, J. L. Biazussi, N. A. V. Bulgarelli, W. D. P. Fonseca, M. S. Castro, E. M. Franklin, A. C. Bannwart, Flow visualization in centrifugal pumps: A review of methods and experimental studies, Journal of Petroleum Science and Engineering (2021) 108582.

[2] N. Paone, M. Riethmuller, R. Van den Braembussche, Experimental investigation of the flow in the vaneless diffuser of a centrifugal pump by particle image displacement velocimetry, Experiments in Fluids 7 (6) (1989) 371–378.

[3] R. Dong, S. Chu, J. Katz, Quantitative visualization of the flow within the volute of a centrifugal pump. part a: Technique, Journal of Fluids Engineering 114 (1) (1992) 390–395.

[4] R. Dong, S. Chu, J. Katz, Quantitative visualization of the flow within the volute of a centrifugal pump. part b: results and analysis, Journal of Fluids Engineering 114 (1) (1992) 396–403.

[5] M. Sinha, J. Katz, Quantitative visualization of the flow in a centrifugal pump with diffuser vanes—i: on flow structures and turbulence, Journal of Fluids Engineering 122 (1) (2000) 97–107.

[6] N. Pedersen, P. S. Larsen, C. B. Jacobsen, Flow in a centrifugal pump impeller at design and off-design conditions—part i: particle image velocimetry (piv) and laser doppler velocimetry (ldv) measurements, Journal of Fluids Engineering 125 (1) (2003) 61–72.

[7] N. Krause, K. Zähringer, E. Pap, Time-resolved particle imaging velocimetry for the investigation of rotating stall in a radial pump, Experiments in Fluids 39 (2) (2005) 192–201.

[8] N. Zhang, B. Gao, Z. Li, D. Ni, Q. Jiang, Unsteady flow structure and its evolution in a low specific speed centrifugal pump measured by piv, Experimental Thermal and Fluid Science 97 (2018) 133–144.

[9] S. Mittag, M. Gabi, Experimental investigation on pump-intake-elbow systems using refraction index matching and tr-spiv, in: 16th International Symposium on Transport Phenomena and Dynamics of Rotating Machinery, 2016.

[10] J. Keller, E. Blanco, R. Barrio, J. Parrondo, Piv measurements of the unsteady flow structures in a volute centrifugal pump at a high flow rate, Experiments in Fluids 55 (10) (2014) 1–14.

[11] O. Akin, D. Rockwell, Flow structure in a radial flow pumping system using high-image-density particle image velocimetry, Journal of Fluids Engineering 116 (1) (1994) 538–544.

[12] P. Dupont, G. Caignaert, G. Bois, T. Schneider, Rotor-stator interactions in a vaned diffuser radial flow pump, in: Fluids Engineering Division Summer Meeting, Vol. 41987, Citeseer, 2005, pp. 1087–1094.

[13] J. Feng, F.-K. Benra, H. Dohmen, Comparison of periodic flow fields in a radial pump among cfd, piv, and ldv results, International Journal of Rotating Machinery 410838.

[14] G. Wuibaut, G. Bois, P. Dupont, G. Caignaert, M. Stanislas, Piv measurements in the impeller and the vaneless diffuser of a radial flow pump in design and off-design operating conditions, Journal of Fluids Engineering 124 (3) (2002) 791–797.

[15] R. Westra, L. Broersma, K. van Andel, N. P. Kruyt, Piv measurements and cfd computations of secondary flow in a centrifugal pump impeller, Journal of Fluids Engineering 132 (6).

[16] A. Dazin, G. Cavazzini, G. Pavesi, P. Dupont, S. Coudert, G. Ardizzon, G. Caignaert, G. Bois, High-speed stereoscopic piv study of rotating instabilities in a radial vaneless diffuser, Experiments in Fluids 51 (1) (2011) 83–93.

[17] X. Luo, Y. Zhang, J. Peng, H. Xu, W. Yu, Impeller inlet geometry effect on performance improvement for centrifugal pumps, Journal of Mechanical Science and Technology 22 (10) (2008) 1971–1976.

[18] J. Pei, F. Zhang, D. Appiah, B. Hu, S. Yuan, K. Chen, S. N. Asomani, Performance prediction based on effects of wrapping angle of a side channel pump, Energies 12 (1) (2019) 139.

[19] X. Li, B. Chen, X. Luo, Z. Zhu, Effects of flow pattern on hydraulic performance and energy conversion characterisation in a centrifugal pump, Renewable Energy 151 (2020) 475–487.

[20] X. Li, H. Chen, B. Chen, X. Luo, B. Yang, Z. Zhu, Investigation of flow pattern and hydraulic performance of a centrifugal pump impeller through the piv method, Renewable Energy 162 (2020) 561–574.

[21] B. Chen, X. Li, Z. Zhu, Investigations of energy distribution and loss characterization in a centrifugal impeller through piv experiment, Ocean Engineering 247 (2022) 110773.

[22] J. Lu, F. Wu, X. Liu, B. Zhu, S. Yuan, J. Wang, Investigation of the mechanism of unsteady flow induced by cavitation at the tongue of a centrifugal pump based on the proper orthogonal decomposition method, Physics of Fluids 34 (10) (2022) 105113.

[23] J. L. Lumley, The structure of inhomogeneous turbulent flows, Atmospheric turbulence and radio wave propagation.

[24] L. Sirovich, Turbulence and the dynamics of coherent structures. i. coherent structures, Quarterly of Applied Mathematics 45 (3) (1987) 561–571.

[25] E. A. Christensen, M. Brøns, J. N. Sørensen, Evaluation of proper orthogonal decomposition–based decomposition techniques applied to parameter-dependent nonturbulent flows, SIAM Journal on Scientific Computing 21 (4) (1999) 1419–1434.

[26] K. Willcox, Unsteady flow sensing and estimation via the gappy proper orthogonal decomposition, Computers & Fluids 35 (2) (2006) 208–226.

[27] M. Ilak, C. W. Rowley, Modeling of transitional channel flow using balanced proper orthogonal decomposition, Physics of Fluids 20 (3) (2008) 034103.

[28] A. Towne, O. T. Schmidt, T. Colonius, Spectral proper orthogonal decomposition and its relationship to dynamic mode decomposition and resolvent analysis, Journal of Fluid Mechanics 847 (2018) 821–867.

[29] X. Ma, G. E. Karniadakis, A low-dimensional model for simulating three-dimensional cylinder flow, Journal of Fluid Mechanics 458 (2002) 181–190.

[30] E. Liberge, A. Hamdouni, Reduced order modelling method via proper orthogonal decomposition (pod) for flow around an oscillating cylinder, Journal of Fluids and Structures 26 (2) (2010) 292–311.

[31] M. El-Adawy, M. R. Heikal, A. R. A. Aziz, I. K. Adam, M. A. Ismael, M. E. Babiker, M. B. Baharom, E. Z. Z. Abidin, On the application of proper orthogonal decomposition (pod) for in-cylinder flow analysis, Energies 11 (9) (2018) 2261.

[32] M. Fogleman, J. Lumley, D. Rempfer, D. Haworth, Application of the proper orthogonal decomposition to datasets of internal combustion engine flows, Journal of Turbulence 5 (1) (2004) 023.

[33] B. Semlitsch, Y. Wang, M. Mihăescu, Flow effects due to pulsation in an internal combustion engine exhaust port, Energy Conversion and Management 86 (2014) 520–536.

[34] B. Semlitsch, M. Mihăescu, Flow phenomena leading to surge in a centrifugal compressor, Energy 103 (2016) 572–587.

[35] W. Shaofei, X. Haowen, Q. Zhongyang, P. Chong, Coherent flow structures near tongue region in a centrifugal fan with forward-curved blades, Journal of Fluids Engineering 145 (3) (2023) 31202.

[36] S. V. Gordeyev, F. O. Thomas, Coherent structure in the turbulent planar jet. part 1. extraction of proper orthogonal decomposition eigenmodes and their self-similarity, Journal of Fluid Mechanics 414 (2000) 145–194.

[37] S. Gordeyev, F. O. Thomas, Coherent structure in the turbulent planar jet. part 2. structural topology via pod eigenmode projection, Journal of Fluid Mechanics 460 (2002) 349–380.

[38] R. Vernet, L. Thomas, L. David, Analysis and reconstruction of a pulsed jet in crossflow by multi-plane snapshot pod, Experiments in fluids 47 (4) (2009) 707–720.

[39] O. Semeraro, G. Bellani, F. Lundell, Analysis of time-resolved piv measurements of a confined turbulent jet using pod and koopman modes, Experiments in fluids 53 (5) (2012) 1203–1220.

[40] R.-H. Zhang, R. Guo, J.-H. Yang, J.-Q. Luo, Inverse method of centrifugal pump impeller based on proper orthogonal decomposition (pod) method, Chinese Journal of Mechanical Engineering 30 (4) (2017) 1025–1031.

[41] R. Guo, R. Li, R. Zhang, Reconstruction and prediction of flow field fluctuation intensity and flow-induced noise in impeller domain of jet centrifugal pump using gappy pod method, Energies 12 (1) (2019) 111.

[42] Z. Zhang, H. Chen, J. Yin, Z. Ma, Q. Gu, J. Lu, H. Liu, Unsteady flow characteristics in centrifugal pump based on proper orthogonal decomposition method, Physics of Fluids 33 (7) (2021) 075122.

[43] R. M. Perissinotto, R. F. L. Cerqueira, W. D. P. Fonseca, W. M. Verde, J. L. Biazussi, A. C. Bannwart, E. M. Franklin, M. S. Castro, Particle image velocimetry in a centrifugal pump: Details of the fluid flow at different operation conditions, Flow Measurement and Instrumentation (2023) 102282.

[44] R. M. Perissinotto, W. D. P. Fonseca, R. F. L. Cerqueira, W. Monte Verde, A. C. Bannwart, E. M. Franklin, M. S. Castro, Particle image velocimetry in a centrifugal pump: Influence of walls on the flow at different axial positions, Journal of Fluids Engineering (2023) 1–34.

[45] W. M. Verde, J. L. Biazussi, N. A. Sassim, A. C. Bannwart, Experimental study of gas-liquid two-phase flow patterns within centrifugal pumps impellers, Experimental Thermal and Fluid Science 85 (2017) 37–51.

[46] R. M. Perissinotto, W. M. Verde, M. S. de Castro, J. L. Biazussi, V. Estevam, A. C. Bannwart, Experimental investigation of oil drops behavior in dispersed oil-water two-phase flow within a centrifugal pump impeller, Experimental Thermal and Fluid Science 105 (2019) 11–26.

[47] R. M. Perissinotto, W. M. Verde, C. E. Perles, J. L. Biazussi, M. S. de Castro, A. C. Bannwart, Experimental analysis on the behavior of water drops dispersed in oil within a centrifugal pump impeller, Experimental Thermal and Fluid Science 112 (2020) 109969.

[48] F. Scarano, M. L. Riethmuller, Iterative multigrid approach in piv image processing with discrete window offset, Experiments in Fluids 26 (6) (1999) 513–523.

[49] X.-D. Liu, Z.-Q. Liu, Q. Zhong, Y.-j. Li, W. Yang, Experimental investigation of relative velocity field based on image rotation method in pump impeller, Flow Measurement and Instrumentation 82 (2021) 102061.

[50] M. Raffel, C. E. Willert, S. T. Wereley, J. Kompenhans, Particle image velocimetry: a practical guide, Springer, 2007.

[51] L. Cordier, M. Bergmann, Proper orthogonal decomposition: an overview, Lecture series 2003-04 on post-processing of experimental and numerical data, Von Karman Institute for Fluid Dynamics. (2003) 46.

[52] K. Taira, S. L. Brunton, S. T. Dawson, C. W. Rowley, T. Colonius, B. J. McKeon, O. T. Schmidt, S. Gordeyev, V. Theofilis, L. S. Ukeiley, Modal analysis of fluid flows: An overview, AIAA Journal 55 (12) (2017) 4013–4041.

[53] J. Weiss, A tutorial on the proper orthogonal decomposition, in: AIAA Aviation 2019 Forum, 2019, p. 3333.

[54] P. Virtanen, R. Gommers, T. E. Oliphant, M. Haberland, T. Reddy, D. Cournapeau, E. Burovski, P. Peterson, W. Weckesser, J. Bright, S. J. van der Walt, M. Brett, J. Wilson, K. J. Millman, N. Mayorov, A. R. J. Nelson, E. Jones, R. Kern, E. Larson, C. J. Carey, İ. Polat, Y. Feng, E. W. Moore, J. VanderPlas, D. Laxalde, J. Perktold, R. Cimrman, I. Henriksen, E. A. Quintero, C. R. Harris, A. M. Archibald, A. H. Ribeiro, F. Pedregosa, P. van Mulbregt, SciPy 1.0 Contributors, SciPy 1.0: Fundamental Algorithms for Scientific Computing in Python, Nature Methods 17 (2020) 261–272. doi:10.1038/s41592-019-0686-2.

[55] C. R. Harris, K. J. Millman, S. J. van der Walt, R. Gommers, P. Virtanen, D. Cournapeau, E. Wieser, J. Taylor, S. Berg, N. J. Smith, R. Kern, M. Picus, S. Hoyer, M. H. van Kerkwijk, M. Brett, A. Haldane, J. F. del Río, M. Wiebe, P. Peterson, P. Gérard-Marchant, K. Sheppard, T. Reddy, W. Weckesser, H. Abbasi, C. Gohlke, T. E. Oliphant, Array programming with NumPy, Nature 585 (7825) (2020) 357–362. doi:10.1038/s41586-020-2649-2.
URL https://doi.org/10.1038/s41586-020-2649-2

[56] J. F. Gülich, Centrifugal pumps, Vol. 2, Springer, 2008.

[57] D. Yuan, J. Deng, R. Han, D. Li, S. Tan, Experimental study on flow structures of central blockage accidents in a rectangular channel using piv and pod, Annals of Nuclear Energy 153 (2021) 108037.

[58] S. B. Pope, S. B. Pope, Turbulent flows, Cambridge university press, 2000.